Electronic properties of graphene with triangular defects in a superhoneycomb arrangement: A first-principles study

Yuta Taguchi,[1,*] Masayuki Toyoda,[1] and Susumu Saito[1,2,3]

[1]*Department of Physics, Tokyo Institute of Technology, 2-12-1 Oh-okayama, Meguro-ku, Tokyo 152-8551, Japan*

[2]*Advanced Research Center for Quantum Physics and Nanoscience, Tokyo Institute of Technology, 2-12-1 Oh-okayama, Meguro-ku, Tokyo 152-8551, Japan*

[3]*Materials Research Center for Element Strategy, Tokyo Institute of Technology, 4259 Nagatsuta-cho, Midori-ku, Yokohama, Kanagawa 226-8503, Japan*

(Received 22 December 2021; revised 5 May 2023; accepted 8 May 2023; published 20 June 2023)

We study the electronic properties of graphene with triangular defects in the superhoneycomb arrangement by performing first-principles calculations within the framework of density functional theory. First, we investigate the band gaps using spin-unpolarized calculations. Interestingly, we find that the system-size dependence of the band gap value is unique and different from the previously known scaling law, which explains the band gap behaviors of various graphene materials with defects. In particular, the defect size dependence of the band gap value shows a different tendency, and thus, we obtain the universal scaling law with respect to the size of the defect and periodicity. We can estimate the band gap values of larger systems using this law without significant computational cost. In addition, we find that the system usually possesses a direct band gap, indicating that it is a promising material for optoelectronics applications. Further, we perform spin-polarized calculations to study stable magnetic states. We find that the ferromagnetic or the antiferromagnetic states are stable when the defect is large. From the analysis of Néel temperature, we also find that the spin-polarized system at 0 K exhibits spin polarization at room temperature when the distance between the defects is rather short. In addition, the band gap value of the spin-polarized system converges to a nonzero value. These findings indicate that further research on graphene with defects is highly significant and necessary for controlling the electronic properties of graphene-based materials.

DOI: 10.1103/PhysRevB.107.235418

I. INTRODUCTION

Graphene, which has been studied theoretically for many years to understand the electronic properties of graphite [1–3], is an interesting metallic monolayer sheet. It has a unique band structure, in which gapless linear dispersion appears in the vicinity of the K and K' points in the first Brillouin zone [1]. Novoselov *et al.* reported the fabrication of graphene by using micromechanical cleavage in 2004 [4]. Thereafter, the experimental studies on the electronic properties of graphene were conducted [5–8], and many interesting properties such as high carrier mobility [5,6], high thermal conductivity [7], quantum Hall effect at room temperature [8], and extraordinary toughness [9,10] were discovered. Although graphene has attracted much attention due to such properties, it cannot be used for ordinary devices where high on/off current ratio is required because graphene does not have a fundamental gap. Therefore, to expand the scope of applications, tuning the electronic properties of graphene is important for realizing next-generation devices.

A promising method to expand the scope of graphene application in devices is the modification of the geometric structures of pristine graphene. The electronic properties of periodically modified graphene have been studied theoretically for the last two decades [11–32], and quantitative electronic structure studies have suggested that periodically modified graphene can be a semiconductor [11,15,16,21,22,24–32]. For example, by applying tight-binding (TB) calculations or first-principles studies in the framework of density functional theory (DFT), graphene with periodically arranged hexagonal, circular, triangular, and rhombus defects is found to be a semiconductor. The band gap (E_g) values of these systems were studied intensively, and a very simple scaling law, $E_g \approx A\sqrt{N_{\rm rem}}/N_{\rm tot}$, was proposed by Pedersen *et al.* when circular defects are arranged in pristine graphene [15]. This formula has been widely used and explains the band gap dependence effectively in several cases where the shape and/or arrangement of defects differ from one another [16,25,27–29]. However, only limited kinds of shapes and lattices of the periodic defects have been investigated in these former studies. Therefore, it is not clear if Pedersen's formula is applicable in the case of a honeycomb lattice where, for example, there are two different defects in a unit cell. According to theoretical studies, magnetic properties can also be changed by periodically arranging defects with zigzag edges in pristine [12–14,16,17,20,27,29,31]. If triangular and rhombus defects with zigzag edges are arranged, the systems are expected to be ferromagnetic (FM) and antiferromagnetic (AM), respectively [16]. It was also found that the magnetic properties

*taguchi.y@stat.phys.titech.ac.jp

 ©2023 American Physical Society

of stable states depend on geometrical parameters, such as the shape and size of defects and the distance between them. Theoretical studies have shown that multiple magnetic properties can be realized by simply creating defects in pristine graphene, and periodically modified graphene is very useful for spintronics applications. However, various periodically modified graphene materials are largely unexplored to date; therefore, we can expect to discover electronic properties that are significant for applications. Hence, theoretical studies of periodically modified graphene are essential.

While various interesting properties of graphene with defects are predicted in DFT studies, it is very difficult to make defects in pristine graphene with the defect size or interdefect distance of the same order ($\sim$ nm) as those assumed in previous DFT studies. Nevertheless, there are many kinds of techniques for arranging defects such as electron-beam lithography [33–35], block copolymer lithography [36–38], self-assembled nanosphere lithography [39–43], and nanoimprint lithography [44,45]. In 2018, Schmidt *et al.* reported that helium ion beam milling should be a promising technique that can realize smaller size defects with shorter interdefect distances [46]. They succeeded in creating defects with a pitch of 18 nm almost completely. In 2020, Liu *et al.* succeeded in creating defects with a pitch of 15 nm using a helium ion beam milling [47]. These distances are only one order of magnitude larger than that dealt with in theoretical investigations. Hence, various periodically modified graphene materials, which have been theoretically studied, may be realized soon. One promising method to produce these materials is the use of a hexegonal boron nitride (*h*-BN) layer, which has a honeycomb lattice structure consisting of alternating boron and nitrogen atoms, and platinum as a catalyst. In 2009, Jin *et al.* successfully resolved triangular defects in monolayer *h*-BN by using an electron beam, keeping the distance between defects equals to several nanometers [48]. Eleven years later, in 2020, Kim *et al.* reported the conversion of *h*-BN to graphene on platinum substrate [49] when the *h*-BN layer was exposed to methane gas. Combining these two experimental results, graphene having triangular defects with a pitch of several nanometers is expected to be produced soon. Therefore, more theoretical research is required to investigate the electronic properties of graphene with triangular defects. Furthermore, even though the fact that the triangular defects can have two different orientations in a honeycomb lattice, such orientation effect has not been studied well [13,14]. With this background, we focused our study on triangular defects having two different directions.

In this paper, using first-principles electronic structure calculations, we investigate the band gap dependence, structure, and energetics of spin-unpolarized and spin-polarized graphene with triangular defects in a superhoneycomb arrangement. We consider the arrangement, where the number of carbon atoms in sublattice A (N_A) is the same as that of carbon atoms in sublattice B (N_B) by introducing two kinds of triangles with opposite directions. Martinazzo *et al.* studied this $N_A = N_B$ case [18]; however, in that study, the size of the triangular defects was fixed. In contrast, in the present paper, we consider various sizes of triangular defects and, as will be discussed below, the size dependence of their electronic structure is found to be strikingly different from that of defective graphene studied previously. First, we focus on the optimized lattice constants obtained by spin-unpolarized calculations. Thereafter, we discuss the scaling laws for E_g obtained by the same calculations. Interestingly, the triangle size dependence of E_g in this paper does not follow the scaling law, $E_g \approx A\sqrt{N_{\rm rem}}/N_{\rm tot}$ [15]. This first counterexample to the scaling law is of high importance since it indicates that periodically modified graphene is an important class of semiconducting materials having rich physics as well as the possibility of electronic structure engineering. Moreover, we studied the details of the electronic structures around the fundamental gap. Finally, we report that the magnetic properties can be tuned by changing the size of the defects and distance between them. We also studied the E_g values of the spin-polarized states.

The remainder of this paper is organized as follows. In Sec. II, the calculation methods used in this paper are described. In Sec. III, the geometries of periodically modified graphene with triangular defects in the superhoneycomb arrangement are explained. In Sec. IV A, the optimized geometries, E_g values, and electronic structures are reported. We also discussed a scaling law for E_g. In Sec. IV B, we introduce the energetics and E_g behavior of spin-polarized graphenes. Finally, we summarized our work in Sec. V.

II. CALCULATION METHODS

In this paper, we performed first-principles total-energy calculations using the generalized gradient approximation (GGA) within the framework of DFT [50,51]. We used the energy functional by Perdew, Burke, and Ernzerhof together with the Vanderbilt ultrasoft pseudopotentials to describe the interactions between the ions and valence electrons [52–54]. The cutoff energies of a plene-wave basis set and a charge density are taken to be 60 Ry and 480 Ry, respectively. In this paper, we used the $L \times L$ ($7 \leqq L \leqq 18$) supercell. The interlayer distance between graphene was maintained to be greater than 10 Å in all systems studied to simulate isolated graphene sheets. The geometries of all the systems studied were fully optimized until the Hellmann-Feynman forces acting on all atoms were less than 0.0001 Ry/bohr. All calculations were performed using the Quantum ESPRESSO package [55]. VESTA [56] was used to visualize the structure of the systems in this paper.

III. SYSTEMS STUDIED

In this paper, we have considered graphene with triangular defects. The carbon atoms at the edges of defects with dangling bonds are terminated by hydrogen atoms. The corners of the triangles are truncated such that the terminating hydrogen atoms on the neighboring sides are not able to come considerably close to each other, as shown in Fig. 1(a). To characterize the defects, an integer l is defined as the defect side length in units of the pristine graphene lattice constant. In this paper, l ranges from 5 to 11. Figure 1(b) shows an example of a superhoneycomb arrangement of triangular defects. Herein, we consider only a hexagonal supercell because it has one degree of freedom (supercell size). However, studying an orthorhombic supercell, which has two degrees of freedom (vertical and horizontal supercell lengths), would

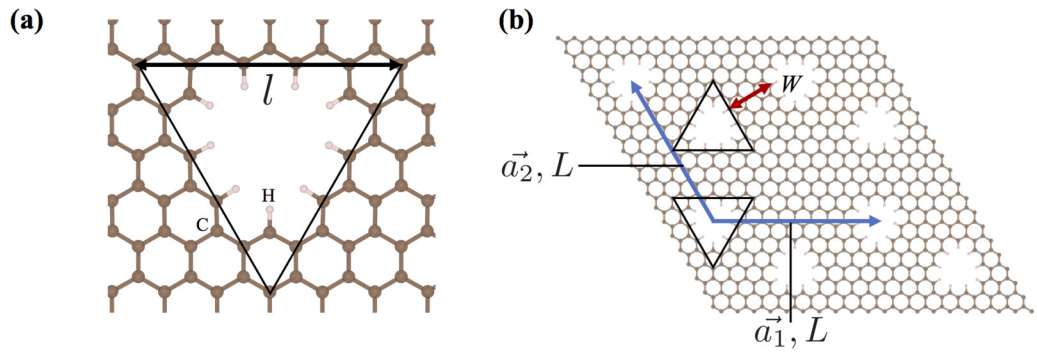

FIG. 1. (a) Truncated triangular defect when $l = 5$. Without removing the carbon atom at each corner of the triangular defect, two hydrogen atoms would be placed considerably closer to each other. (b) System for $(l, L, W) = (5, 10, 5)$. In both figures, pink and brown balls represent hydrogen and carbon atoms, respectively. Definitions of l, L, and W are given in Sec. III.

be an interesting future work. The unit cell of the system is a rhombus with $\vec{a}_1$ and $\vec{a}_2$ as primitive translation vectors. Two types of triangles of the same size exist: One is upward and the other is downward in the unit cell. The defects are arranged such that the regular triangle centers form a honeycomb lattice. To characterize the superhoneycomb arrangement, we define two integers, W and L, as the subribbon width in units of the C–C bond length and the length of $\vec{a}_1$ ($\vec{a}_2$) in units of the pristine graphene lattice constant. Because $W = L - l$ is always satisfied and we can identify graphene with triangular defects in the superhoneycomb arrangement by a pair of integers (l, L), we use the label "(l, L) graphene." Note that some (l, L) graphenes are not allowed, for example, (5,8) graphene. When the remainder of l divided by 3 is 0, 1, and 2, that of L is always 2, 0, and 1, respectively, in this honeycomb arrangement. In addition, L must be larger than $l + 2$. For example, $(l, L) = (5, 7), (5, 10), (5, 13)$... are allowed when $l = 5$. Because graphene with defects often exhibits magnetism, we performed both spin-unpolarized and spin-polarized calculations for the selected (l, L) graphene.

IV. RESULTS AND DISCUSSION

A. Spin-unpolarized graphene

1. Structural properties

Table I shows the optimized lattice constants of (l, L) graphenes (a) by spin-unpolarized calculations and the effect of arranging the defects on the lattice constant ($a - L \times a_0$), where the lattice constant of pristine graphene (a_0) is obtained using the same methodology and is in good agreement with the experimental value [57] as well as the calculated values [58–61]. It is to be noted that the lattice constants obtained using GGA calculations are usually overestimated, and the values of $a - L \times a_0$ are always positive. This is because of the existence of armchair edges at the corners of the triangular defects (Fig. S1 in Supplemental Material [62]). The C–C bond at the armchair edge is slightly longer than that of pristine graphene [63]. In the present system, the C–C bond at the armchair edge (d_A) is also longer than that of pristine graphene (1.423 Å) as shown in Table S1 [62]. This can be attributed to $(a - L \times a_0) > 0$ observed in the present systems. We found that $(a - L \times a_0)$ monotonically decreases with L, and a is independent of l when L is fixed. Therefore, two-dimensional van der Waals heterostructures consisting only of (l, L) graphene with different values of l can have a commensurate lattice owing to their negligible lattice mismatch. As discussed later, the spin-polarization calculation is performed for $W = 2$ and 5. It was found that the lattice constants of spin-polarized graphene were nearly the same as those of spin-unpolarized graphene.

2. Scaling law of the band gap values

We calculated the band gap (E_g) values of the selected (l, L) graphene and they varied from 0.01 eV [(11,13)

TABLE I. Lattice constants (in Å) of the spin-unpolarized graphenes. Differences between a and $L \times a_0$ are also shown. Note that L is 1 in the case of pristine graphene.

Graphene				
l	L	W	Lattice constant a	$a - L \times a_0$
5	7	2	17.335	0.089
	10	5	24.696	0.060
	13	8	32.073	0.046
	16	11	39.455	0.038
6	8	2	19.793	0.084
	11	5	27.157	0.057
	14	8	34.537	0.047
	17	11	41.921	0.040
7	9	2	22.249	0.077
	12	5	29.615	0.052
	15	8	36.998	0.044
	18	11	44.384	0.039
8	10	2	24.706	0.070
	13	5	32.073	0.047
	16	8	39.458	0.041
9	11	2	27.162	0.062
	14	5	34.532	0.042
10	12	2	29.618	0.054
	15	5	36.991	0.037
11	13	2	32.078	0.051
	16	5	39.449	0.031
Pristine graphene			2.464(=a_0)	0

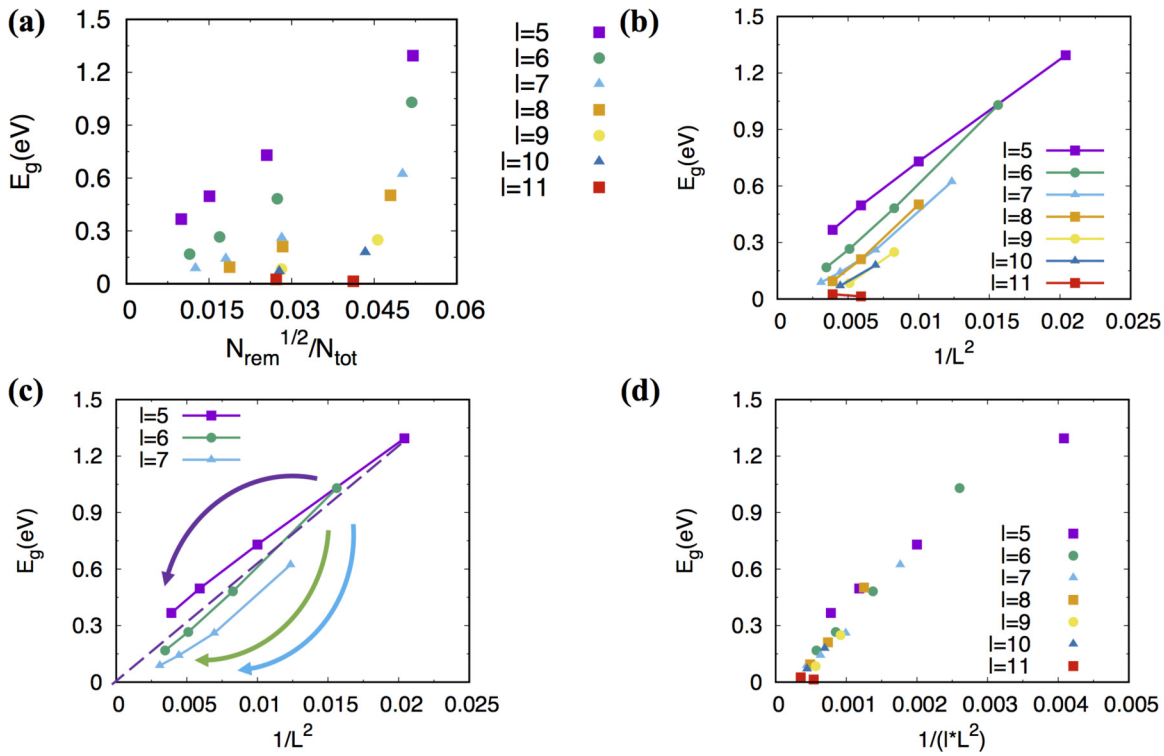

FIG. 2. Band gap (E_g) values of the systems as a function of (a) $\sqrt{N_{\rm rem}}/N_{\rm tot}$ and (b) $1/L^2$, respectively. (c) E_g values of the (5,L), (6,L) and (7,L) graphenes as a function of $1/L^2$, together with the purple dotted line representing a linear curve connecting origin and the (5,7) graphene value. (d) E_g values of the systems as a function of $1/(l \times L^2)$.

graphene] to 1.29 eV [(5,7) graphene]. It should be noted that the GGA value of E_g is usually underestimated; therefore, the actual value of E_g may vary over a wider range than 2 eV. Further studies are required for the quantitative estimation of E_g, but it is possible to discuss the qualitative behavior of E_g as a function of l and L. In the following, we describe this behavior in detail.

In previous studies, it was found that the calculated values of E_g of graphene with circular defects are often found around a straight line when plotted as a function of $\sqrt{N_{\rm rem}}/N_{\rm tot}$, where $N_{\rm rem}$ is the number of carbon atoms removed when the defects are made and $N_{\rm tot}$ is the number of carbon atoms in a unit area before the periodic defects are made [15]. This interesting result was also obtained in the case of different defect shapes. However, as shown in Fig. 2(a), E_g of the (l, L) graphenes is not on a single line but on several lines with different slopes depending on l. The E_g values obtained in this paper did not fully follow the previous scaling law. In fact, there was a report that the band gap value deviates systematically from Pedersen's formula in a system with a triangular lattice of large hexagonal defects [27]. The present results now more clearly shows that there are a wide variety of the band gap behaviors in periodically modified graphene.

To analyze the difference of the E_g behavior in more detail, we plotted the E_g values as a function of $1/L^2$ for each l, as shown in Fig. 2(b). Interestingly, the value of E_g with a fixed L decreases monotonically with the defect side length l, for example, for the (5,10) and (8,10) graphenes. According to the previous scaling law, the value of E_g with a fixed L should monotonically increase with l because increasing l and fixing L means increasing $N_{\rm rem}$ with a fixed $N_{\rm tot}$. Hence, the E_g dependence of (l, L) graphene strikingly contradicts the previously proposed scaling law. In contrast, the value of E_g with constant l obtained in this paper linearly increases as $1/L^2$, which is nearly the same as the linear scaling law proposed by Sakurai *et al.* [24] and Pedersen *et al.*, $E_g \propto 1/N_{\rm tot} \propto 1/L^2$ with a fixed l ($N_{\rm rem}$) [15].

To analyze the E_g behavior of (l, L) graphene, we further discuss a more accurate scaling function of the present systems with a constant l. Here, we study cases for $l = 5, 6$, and 7 because there are four data points per l, and, hence, more accurate scaling functions can be obtained. As shown in Fig. 2(c), the lines connecting the (5,L), (6,L), and (7,L) graphene values (purple, green, and light blue solid lines, respectively) are convex upward, downward, and downward, respectively. We assumed that the E_g value with a constant l is 0 when $L = \infty$ ($1/L^2 = 0$) because the system can be regarded as pristine graphene ($E_g = 0$). For this assumption, we set a simple scaling function of the band gap values with a fixed l as follows:

$$E_{l,L,g} = \frac{\lambda_l}{L^{\alpha_l}}\ \text{eV}, \tag{1}$$

where λ_l and α_l are positive constants ($\alpha_l < 2$ for $l = 5$, and $\alpha_l > 2$ for $l = 6, 7$) and $E_{l,L,g}$ is the E_g value of (l, L) graphene. To determine λ_l and α_l, we take the logarithm of both sides of Eq. (1):

$$\log_{10} E_{l,,L,g} = -\alpha_l \log_{10} L + \log_{10} \lambda_l. \tag{2}$$

TABLE II. Constants α_l and $\log_{10}\lambda_l$ obtained by the least-squares method applied to four data corresponding to $W = L - l =$ 2, 5, 8, and 11, with l fixed.

l	α_l	$\log_{10}\lambda_l$
5	1.52	1.39
6	2.41	2.19
7	2.83	2.49

Next, we applied the least-squares method to Eq. (2). We obtain α_l and $\log_{10}\lambda_l$ as the slope of the line and intercept, respectively. Table II lists the combinations of α_l and $\log_{10}\lambda_l$ for each l. It is found that α_l strongly depends on l (the size of defects) and monotonically increases with l. Finally, to derive the scaling function, Eq. (1) for each l, we transform $\log_{10}\lambda_l$ into λ_l, for example, $\log_{10}\lambda_5 = 1.39$ gives $\lambda_5 \sim 24.5$. Then, the scaling functions can be expressed as

$$E_{5,L,g} = \frac{24.5}{L^{1.52}}\ \text{eV}, \tag{3a}$$

$$E_{6,L,g} = \frac{155}{L^{2.41}}\ \text{eV}, \tag{3b}$$

$$E_{7,L,g} = \frac{309}{L^{2.83}}\ \text{eV}. \tag{3c}$$

Although the gap value is underestimated in LDA and GGA, the deviation from the actual values is rather systematic; therefore, the gap value variation given in LDA (GGA) for one class of materials can even be quantitatively reliable in some cases. For example, it is known that LDA reproduces the ribbon width dependence of E_g obtained by the GW approximation in the cases of armchair and zigzag graphene nanoribbons (ZGNRs) [64]. Therefore, these three equations can provide quantitatively reliable gap value variation as a function of L as well as l. For each l, we obtained α_l and $\log_{10}\lambda_l$ from two E_g values ($W = L - l = 2, 5$) and three E_g values ($W = L - l = 2, 5, 8$) to check the convergence with respect to the number of E_g values used. In the case of $l = 5$, α_5 is 1.60 and 1.55 for two and three values, respectively. Therefore, α_5 of 1.52 (Table II) seems to nearly converge. Interestingly, the convergence of α_6 is even faster [$\alpha_6 = 2.38$ (two values) and $\alpha_6 = 2.42$ (three values)]. Besides, in the case of $l = 7$, α_7 should take a smaller value than 2.82 (Table II) [$\alpha_7 = 3.04$ (two values) and $\alpha_7 = 2.90$ (three values)].

Because $E_{11,L,g} \sim 0$, it would be sufficient to consider a scaling law in the case of $5 \leqq l \leqq 10$. To obtain higher E_g values for each l, we should use the TB method, which can treat a system with thousands of atoms in the unit cell. Therefore, it is important to investigate the E_g scaling laws by performing TB calculations for a wider range of L values.

Finally, we constructed a scaling function for the E_g values for (l, L) graphene. From the interesting l dependence of the E_g values with a fixed L, we set $1/(l \times L^2)$ to the horizontal axis and plotted the E_g values obtained in this paper, as shown in Fig. 2(d). Notably, these E_g values were found around a straight line. This behavior is in sharp contrast to the scaling law $E_g \approx A\sqrt{N_{\text{rem}}}/N_{\text{tot}}$, which is nearly proportional to l/L^2 ($N_{\text{rem}} = 2l^2 - 4l - 4$, $N_{\text{tot}} = 2L^2$ in this paper). Therefore, the E_g value of the present (l, L) graphene system exhibits a unique defect size dependence. Because the E_g value should be 0 when $1/(l \times L^2)$ is 0 (the pristine graphene limit), we set the scaling function as

$$E_{l,L,g} = \frac{\lambda}{l \times L^2}, \tag{4}$$

where λ is the positive constant. By applying the least-squares method to Eq. (4), we obtain the scaling function, which is expressed as

$$E_{l,L,g} = \frac{337}{l \times L^2}\ \text{eV}. \tag{5}$$

On adding the intercept to Eq. (4) and applying the least-squares method, we obtain the scaling function:

$$E_{l,L,g} = \left[\frac{370}{l \times L^2} - 0.0586\right]\text{eV}. \tag{6}$$

The coefficients of determination without and with considering the intercept were 0.937 [Eq. (5)] and 0.949 [Eq. (6)], respectively. Therefore, Eq. (6) should provide a better estimation of the E_g value for the finite L studied here. Conversely, Eq. (5) should better estimate the E_g value for sufficiently large L. Although these Eqs. (5) and (6) apply only to graphene with triangular defects in a superhoneycomb arrangement at present, they must be very useful for controlling E_g when (l, L) graphene is realized. Some E_g values, such as $E_{5,16,g}$, are slightly different from the fitting line; therefore, the scaling function obtained with a fixed l may yield more accurate E_g values. Nonetheless, $1/(l \times L^2)$ is a good scaling function to explain $E_{l,L,g}$ behaviors. Although the experimental production of the superhoneycomb arrangement of the triangular defects has not been reported yet, the comparison of the prediction using the above scaling expressions with future experimental results will further clarify the effect of the inhomogeneity of defects and the effect of the deviations of the defect positions from the ideal lattice sites.

Further, we discuss the physical origin of this unique l dependence of E_g values. Figure 3 shows the electronic states of the lowest-unoccupied (LU) and highest-occupied (HO) bands at the Γ point in two different defected graphenes, (5,16) graphene and (11,16) graphene, where they have different l but share the common L. The LU and HO bands are localized at the zigzag edges of the triangular defects and the band gap arises from the bonding/antibonding-type splitting. However, the states in (11,16) graphene, where the defect intervals (W) are short, are strongly localized at the edge of the carbon atoms, whereas those in (5,16) graphene are more extended over the inner carbon atoms. Therefore, the edge states are hybridized with the neighboring states and the splitting of $E_g = 0.37$ eV occurs in (5,16) graphene. In contrast, in (11,16) graphene, the edge states are barely hybridized with neighbors and exhibit an almost closed band gap of $E_g = 0.02$ eV. It is known that the band gap value in ZGNRs is inversely proportional to the ribbon width (W) [65,66]. Because the l dependence of the E_g value is completely opposite in (l, L) graphenes, it is suggested that graphene with triangular defects in a superhoneycomb arrangement cannot be simply regarded as a collection of ZGNR. It is intriguing to clarify the difference between the triangular networks of interconnected ZGNR and isolated ZGNR. However, as this exceeds the scope of this paper, we leave it as a future study.

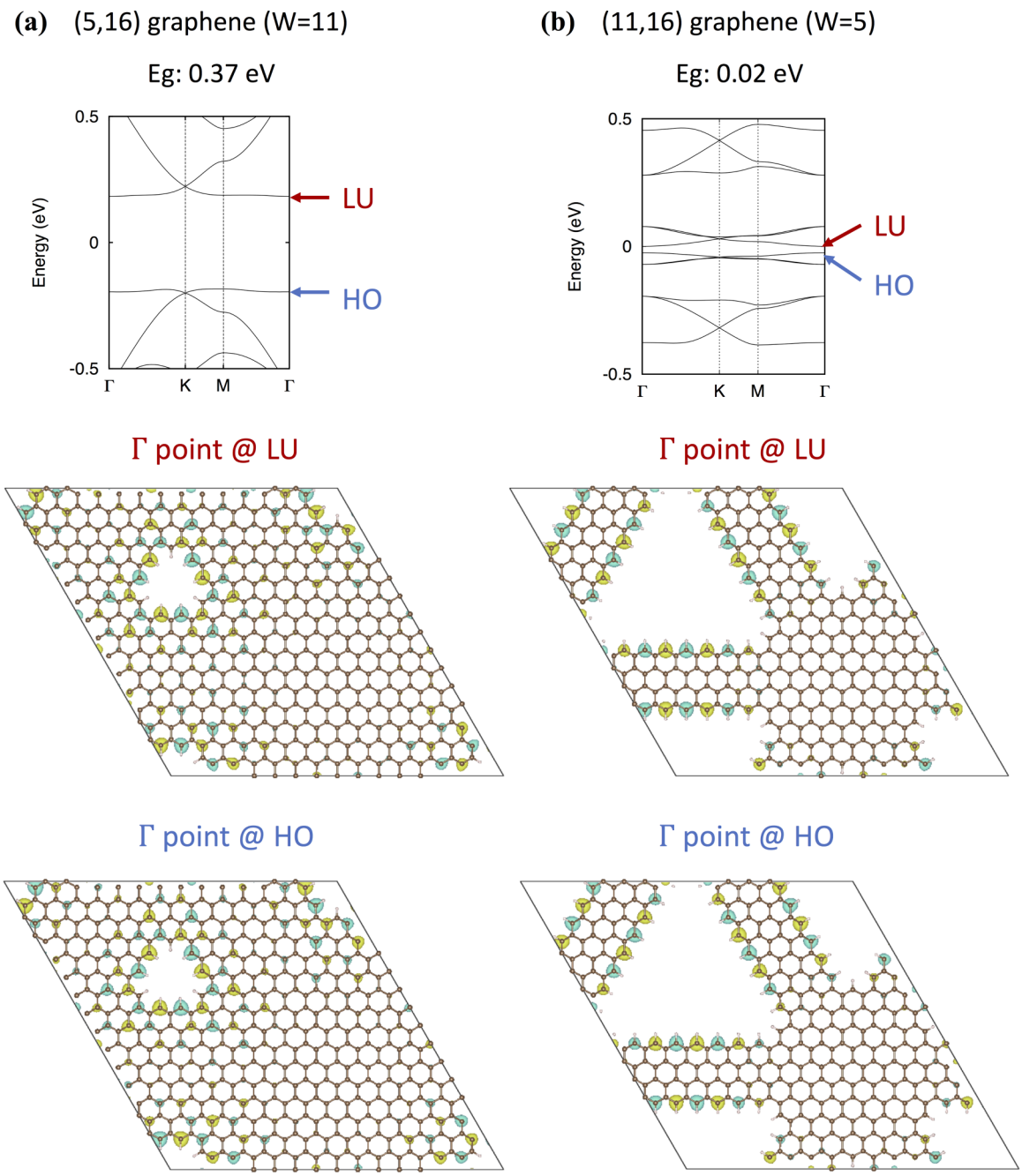

FIG. 3. Electronic structures and electronic states of (a) (5,16) and (b) (11,16) graphene. In the electronic structure, the middle of the CBM (conduction band minimum) and the VBM (valence band maximum) is set to zero. In the spatial distribution of the lowest-unoccupied (LU) state and the highest-occupied (HO) state, sign differences of the wave functions are shown by two colors.

The results in this section indicate that the scaling law depends on the defect shape and arrangement. Especially, the defect size (N_{rem}) dependence of the present scaling law is strikingly different from that of Pedersen's scaling law. Hence, studying the electronic properties of periodically modified graphene with various defects is essential for exploring the physics and applications of graphene.

3. Electronic structure and transition types

The electronic structures of (l, L) graphene ($l = 5, 6, 7,$ and 8) are shown in Fig. 4 and Fig. S2 of the Supplemental Material [62]. The energy bands of (5,L) and (7,L) graphenes have similar dispersions near the fundamental gap. The LU (HO) and second LU (HO) bands usually cross at the K point, and the bands near these cross points have nearly linear dispersions, although the gradients of the two lines change abruptly around the crossing points. This feature was also observed in a previous study [18]. We also found that the energy bands of (6,L) and (8,L) graphenes have similar dispersions near the fundamental gap as well. In these cases, on the other hand, the second and third lowest LU (HO) bands cross at the K point and the bands near these cross points have nearly linear dispersions. This tendency is not observed in the electronic

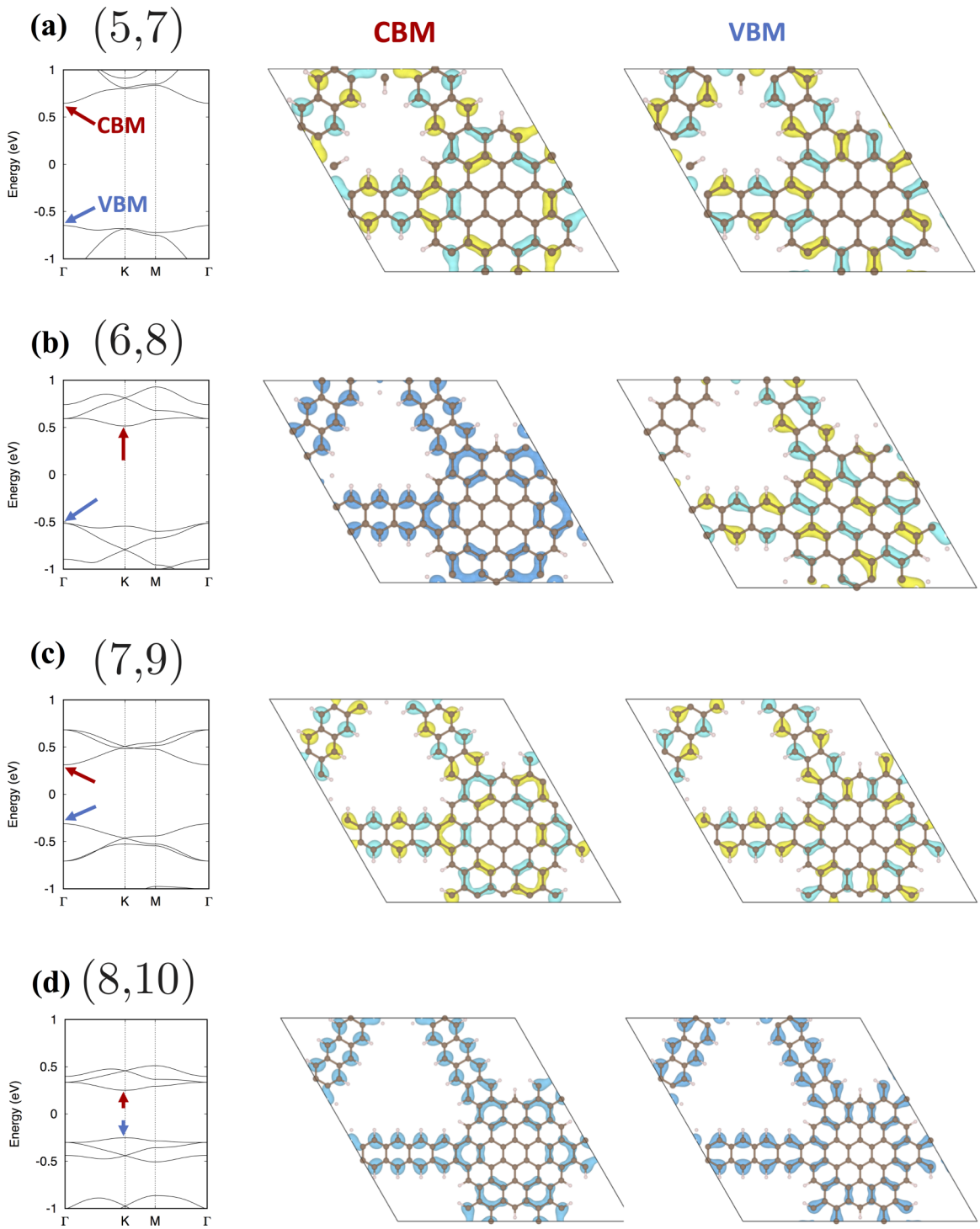

FIG. 4. Electronic structures of (a) (5,7) graphene, (b) (6,8) graphene, (c) (7,9) graphene, and (d) (8,10) graphene. The middle of the CBM and the VBM is set to zero. The red and blue arrows denote the positions of the CBM and VBM, respectively. Contours of the squared wave functions of CBM and VBM states at certain values are shown. In the case of the Γ point, sign differences of the wave functions are shown by two colors.

structures of the (l, L) graphenes ($l = 5, 7$). Hence, the electronic structure near the fundamental gap can be characterized by the parity of l. Electronic states near the fundamental gap are also characterized by the parity of l. As shown in Figs. S3 and S4 of the Supplemental Material [62], the wave functions at the Γ point of the LU (HO) and second LU (HO) bands are bulklike states in the cases of (6,8) and (8,10) graphene, whereas they are almost defect states in the cases of (5,7) and (7,9) graphene. Clarifying the physical origin of these differences is an interesting topic for future work. In Fig. 4, the spatial distributions of the HO and LU bands at their maximum and minimum points (VBM and CBM), respectively,

TABLE III. Variations of LU and HO eigenvalues along the $\Gamma - K - M - \Gamma$ (meV). An eigenvalue is measured from Γ point. $\nearrow$ and $\searrow$ represent monotonically increasing and decreasing, respectively. For example, $\searrow$ 156 $\nearrow$ between K and M points in this table means the eigenvalue decreases monotonically from the K point to local minimum point of 156 meV, and then increases monotonically up to the M point. Bold letters represent local minimum points in LU bands and local maximum points in HO bands.

(l, L)	band	Γ		K		M		Γ
(5,7)	LU	**0 (CBM)**	$\nearrow$	160	$\searrow$ **156** $\nearrow$	190	$\searrow$	**0 (CBM)**
(5,10)		**0 (CBM)**	$\nearrow$	81.4	$\searrow$ **58** $\nearrow$	58.3	$\searrow$	**0 (CBM)**
(5,13)		**0 (CBM)**	$\nearrow$	52.1	$\searrow$	18.1	$\searrow$	**0 (CBM)**
(5,16)		**0 (CBM)**	$\nearrow$	38.7	$\searrow$	**3.8**	$\nearrow$ 4.5 $\searrow$	**0 (CBM)**
(5,7)	HO	**0 (VBM)**	$\searrow$ −49.3 $\nearrow$ **−32.3** $\searrow$	−35.6	$\nearrow$ **−33.8** $\searrow$	−76.3	$\nearrow$	**0 (VBM)**
(5,10)		**0 (VBM)**	$\searrow$ −12.6 $\nearrow$ **−6.1** $\searrow$	−16.8	$\nearrow$ **−8.0** $\searrow$	−15.4	$\searrow$ −16.0 $\nearrow$	**0 (VBM)**
(5,13)		**0**	$\searrow$ −1.7 $\nearrow$ **6.4** $\searrow$	−7.1	$\nearrow$ **6.7 (VBM)** $\searrow$	6.0	$\searrow$ −1.9 $\nearrow$	**0**
(5,16)		**0**	$\searrow$ −0.1 $\nearrow$ **9.6** $\searrow$	−4.2	$\nearrow$	**12.0 (VBM)**	$\searrow$ −0.1 $\nearrow$	**0**
(6,8)	LU	**0**	$\nearrow$ 4.0 $\searrow$	**−77.1 (CBM)**	$\nearrow$	−7.7	$\nearrow$ 10.9 $\searrow$	**0**
(6,11)		**0 (CBM)**	$\nearrow$ 44.5 $\searrow$	**36.4**	$\nearrow$	76.8	$\searrow$	**0 (CBM)**
(6,14)		**0 (CBM)**	$\nearrow$ 63.0 $\searrow$	**61.8**	$\nearrow$	91.5	$\searrow$	**0 (CBM)**
(6,17)		**0 (CBM)**	$\nearrow$ 65.8 $\searrow$	**65.6**	$\nearrow$	88.9	$\searrow$	**0 (CBM)**
(6,8)	HO	**0 (VBM)**	$\searrow$ −48.8 $\nearrow$	**−29.3**	$\searrow$	−85.1	$\nearrow$	**0 (VBM)**
(6,11)		**0 (VBM)**	$\searrow$ −80.1 $\nearrow$	**−78.6**	$\searrow$	−111	$\nearrow$	**0 (VBM)**
(6,14)		**0 (VBM)**	$\searrow$	−85.7	$\searrow$	−109	$\nearrow$	**0 (VBM)**
(6,17)		**0 (VBM)**	$\searrow$	−80.2	$\searrow$	−97.8	$\nearrow$	**0 (VBM)**
(7,9)	LU	**0 (CBM)**	$\nearrow$	171	$\nearrow$ 177 $\searrow$	166	$\searrow$	**0 (CBM)**
(7,12)		**0 (CBM)**	$\nearrow$	103	$\searrow$	61.3	$\searrow$	**0 (CBM)**
(7,15)		**0 (CBM)**	$\nearrow$	67.2	$\searrow$	26.9	$\searrow$	**0 (CBM)**
(7,18)		**0 (CBM)**	$\nearrow$	50.5	$\searrow$	14.3	$\searrow$	**0 (CBM)**
(7,9)	HO	**0 (VBM)**	$\searrow$	−153	$\nearrow$	−129	$\nearrow$	**0 (VBM)**
(7,12)		**0 (VBM)**	$\searrow$	−68.1	$\nearrow$	−43.3	$\nearrow$	**0 (VBM)**
(7,15)		**0 (VBM)**	$\searrow$	−34.2	$\nearrow$	−14.9	$\nearrow$	**0 (VBM)**
(7,18)		**0 (VBM)**	$\searrow$	−19.4	$\nearrow$	−5.2	$\nearrow$	**0 (VBM)**
(8,10)	LU	0	$\searrow$	**−85.7 (CBM)**	$\nearrow$	−42.6	$\nearrow$	0
(8,13)		**0**	$\nearrow$ 5.3 $\searrow$	**−7.9 (CBM)**	$\nearrow$	14.8	$\searrow$	**0**
(8,16)		**0 (CBM)**	$\nearrow$ 11.4 $\searrow$	**8.6**	$\nearrow$	23.7	$\searrow$	**0 (CBM)**
(8,10)	HO	0	$\nearrow$	**49.8 (VBM)**	$\searrow$	15.7	$\searrow$ −0.4 $\nearrow$	0
(8,13)		**0 (VBM)**	$\searrow$ −9.9 $\nearrow$	**−3.0**	$\searrow$	−18.3	$\nearrow$	**0 (VBM)**
(8,16)		**0 (VBM)**	$\searrow$ −14.3 $\nearrow$	**−13.4**	$\searrow$	−21.7	$\nearrow$	**0 (VBM)**
(9,11)	LU	**0 (CBM)**	$\nearrow$ 109 $\searrow$	**108**	$\nearrow$ 120 $\searrow$	116	$\searrow$	**0 (CBM)**
(9,14)		**0 (CBM)**	$\nearrow$	58.0	$\searrow$	35.1	$\searrow$	**0 (CBM)**
(9,11)	HO	**0 (VBM)**	$\searrow$	−119	$\nearrow$	−99.6	$\nearrow$	**0 (VBM)**
(9,14)		**0 (VBM)**	$\searrow$	−37.7	$\nearrow$	−26.3	$\nearrow$	**0 (VBM)**
(10,12)	LU	0	$\searrow$	**−63.3 (CBM)**	$\nearrow$	−34.6	$\nearrow$	0
(10,15)		**0**	$\nearrow$ 0.5 $\searrow$	**−9.7 (CBM)**	$\nearrow$	1.7	$\nearrow$ 1.9 $\searrow$	**0**
(10,12)	HO	0	$\nearrow$	**46.8 (VBM)**	$\searrow$	24.4	$\searrow$	0
(10,15)		**0**	$\searrow$ −0.9 $\nearrow$	**5.7 (VBM)**	$\searrow$	−0.5	$\searrow$ −1.6 $\nearrow$	**0**
(11,13)	LU	**0 (CBM)**	$\nearrow$ 71.9 $\searrow$	**71.0**	$\nearrow$ 82.7 $\searrow$	81.8	$\searrow$	**0 (CBM)**
(11,16)		**0 (CBM)**	$\nearrow$	29.5	$\searrow$	18.5	$\searrow$	**0 (CBM)**
(11,13)	HO	**0 (VBM)**	$\searrow$	−75.6	$\searrow$ −76.8 $\nearrow$	−73.6	$\nearrow$	**0 (VBM)**
(10,16)		**0 (VBM)**	$\searrow$	−16.8	$\nearrow$	−13.2	$\nearrow$	**0 (VBM)**

are shown for (5,7), (6,8), (7,9), and (8,10) graphene. It was found that these wave functions are mostly localized near defects, while the wave function at the VBM in (6,8) graphene is extended.

In addition to the E_g value, the transition type of (l, L) graphene is crucial for various applications such as optoelectronic devices. Interestingly, in the present paper, as many as 17 (l, L) graphenes were direct gap semiconductors, while the remaining four (5,13), (5,16), (6,8), and (8,13) were indirect gap semiconductors. This result indicated that (l, L) graphene is a promising material for optoelectronic applications. In Table III, the locations of the CBM and the VBM are summarized, together with the change in the eigenvalues of the LU and the HO bands along the $\Gamma - K - M - \Gamma$ line. CBM and VBM must be local minimum points in the LU band and local maximum point in the HO band, respectively. Hence,

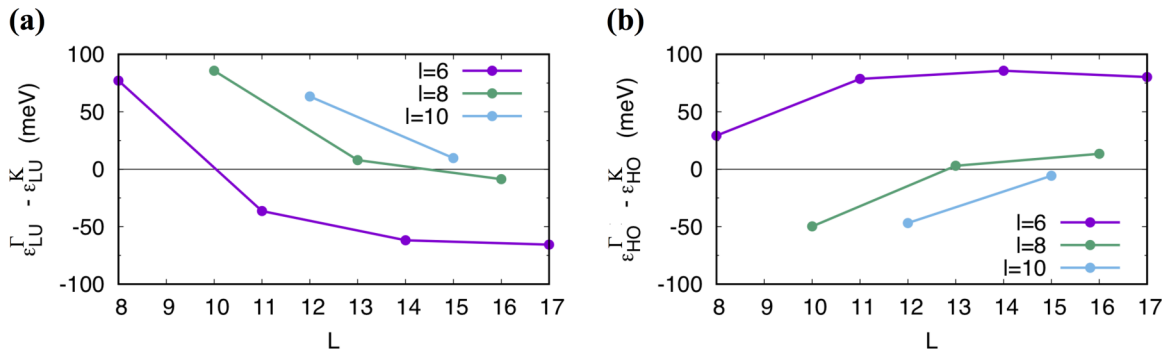

FIG. 5. (a) $\epsilon^{\Gamma}_{\mathrm{LU}} - \epsilon^{K}_{\mathrm{LU}}$ and (b) $\epsilon^{\Gamma}_{\mathrm{HO}} - \epsilon^{K}_{\mathrm{HO}}$ values for the (l, L) graphenes when l is even.

we focus on the eigenvalues of the minimum points in the LU band and maximum points in HO band later in this section. Here, we define ϵ_{VBM}, $\epsilon^{\Gamma}_{\mathrm{HO}}$, $\epsilon^{K}_{\mathrm{HO}}$, and $\epsilon^{M}_{\mathrm{HO}}$ as the eigenvalues at the VBM and at the Γ, K, and M points in the HO band. Similarly, we define ϵ_{CBM}, $\epsilon^{\Gamma}_{\mathrm{LU}}$, $\epsilon^{K}_{\mathrm{LU}}$, and $\epsilon^{M}_{\mathrm{LU}}$ as the eigenvalues at the CBM and at the Γ, K, and M points in the LU band, respectively.

Interestingly, (l, L) graphene always possesses a direct gap at the Γ point when l is odd, except for $l = 5$. As shown in Table III, the local minimum point in the LU band and the local maximum point in the HO band are located only at the Γ point in most cases when l is odd ($l \geqq 7$). As a result, the fundamental gap remains direct when we increase L with the fixed l. However, when l is 6 or 8, the local minimum points in the LU band are located at both the Γ and K points except for the (8,10) graphene. The differences, $\epsilon^{\Gamma}_{\mathrm{LU}} - \epsilon^{K}_{\mathrm{LU}}$, are 77.1 meV, −36.4 meV, −61.8 meV, and −65.6 meV in the cases of the (6,8), (6,11), (6,14), and (6,17) graphenes, respectively. Additionally, $\epsilon^{\Gamma}_{\mathrm{LU}} - \epsilon^{K}_{\mathrm{LU}}$ are 85.7 meV, 7.9 meV, and −8.6 meV for (8,10), (8,13), and (8,16) graphene, respectively. As shown in Fig. 5(a), $\epsilon^{\Gamma}_{\mathrm{LU}} - \epsilon^{K}_{\mathrm{LU}}$ monotonically decreases with L; therefore, the CBM changes from the K point to the Γ point. Next, the local maximum point in the HO band was located only at the Γ point when L increases for $l = 6$. However, for $l = 8$, the local maximum points are located at both Γ and K points when L increases. The $\epsilon^{\Gamma}_{\mathrm{HO}} - \epsilon^{K}_{\mathrm{HO}}$ values are −49.8 meV, 3.0 meV and 13.4 meV with the (8,10), (8,13), and (8,16) graphenes [Fig. 5(b)], respectively. Thus, when the VBM changes from the K point to the Γ point for $l = 8$, the VBM stays at the Γ point for $l = 6$. Therefore, when l is 6 or 8, a change from the direct (indirect) to the indirect (direct) gap occurs, and the fundamental gap is direct at the Γ point for a large L. When l is 10, the (10,12) and (10,15) graphenes are direct gap semiconductors at the K point, but $\epsilon_{\Gamma,\mathrm{LU}} - \epsilon_{K,\mathrm{LU}}$ and $\epsilon_{\Gamma,\mathrm{HO}} - \epsilon_{K,\mathrm{HO}}$ increases and decreases as a function of L, respectively (Fig. 5). The CBM and VBM of $(10, L)$ graphene for $L \geqq 18$ may change from the K point to the Γ point. When l is 5, the minimum points in the LU band and the maximum points in the HO band are sometimes not located at high-symmetry points (Γ, K, M). In the case of (5,13) and (5,16) graphene, VBM is not located at the Γ point, and these two systems are indirect gap semiconductors.

B. Spin-polarized graphene

1. Stable magnetic states

By considering the spin degree of freedom, we sometimes obtain not only nonmagnetic (NM) state but also stable FM and AM states in (l, L) graphene. As shown in Fig. 6, only the NM state is obtained for the small-l case, whereas AM and sometimes additional FM states are obtained for the large-l case. Theoretically, the AM state is found to be more stable than the FM state. This result is consistent with Lieb's theorem [67]. According to this theorem, the total magnetic moment (M) of the ground state can be written as $M = (N_A - N_B)\mu_B$ in the case of a bipartite lattice, where N_A and N_B are the numbers of atoms belonging to the A and B sublattices, respectively. The (l, L) graphene can be regarded as a bipartite lattice, and

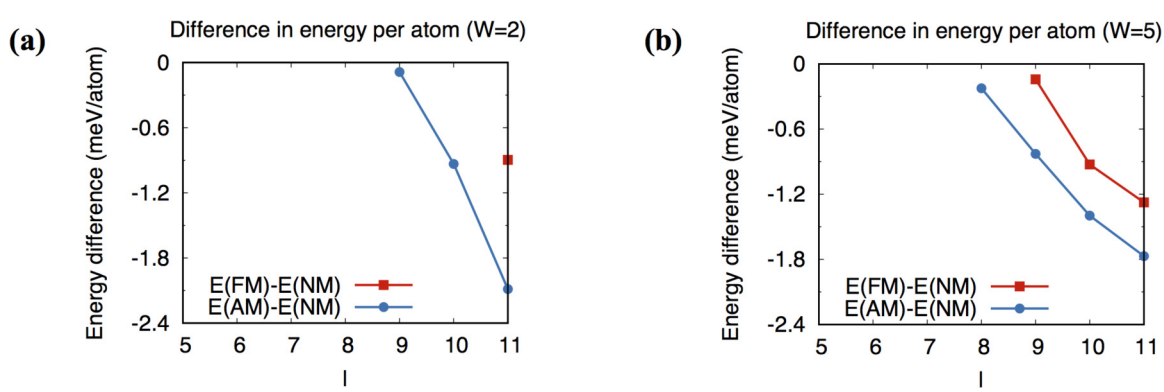

FIG. 6. Energy difference per atom between the stable magnetic state and nonmagnetic state. E(NM), E(FM), and E(AM) represent the energy per atom of the nonmagnetic, ferromagnetic, and antiferromagnetic states, respectively. It is to be noted that $W = L - l$.

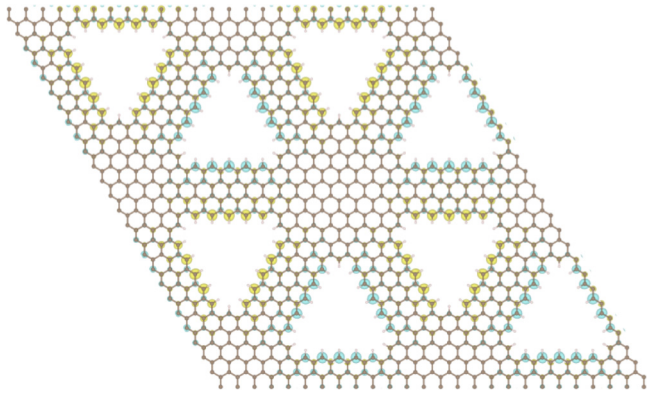

FIG. 7. Spin distribution of AM state in (8,13) graphene. Positive and negative values of the spin density are shown by yellow and light blue colors, respectively.

the number of carbon atoms in two sublattices (N_A and N_B) are the same. Hence, the AM state ($M = 0$) is more stable than the FM state ($M \neq 0$). Further, we show the spin distribution of the AM state for (8,13) graphene in Fig. 7. There are two primary characteristics. First, the spin density is larger near the defect, and smaller far from the defect. Second, the sign of the magnetic moment in one sublattice is opposite to that in the other sublattice. The AM (l, L) graphene studied always has these characteristics. This result is consistent with a previous work by Yu *et al.* [13]. Finally, why (l, L) graphenes exhibit magnetism when l is large can be discussed. As shown in Fig. S1 [62], armchair edges exist at the corners of triangular defects. It is well-known that armchair graphene nanoribbons do not exhibit spin polarization [68]. In fact, the spin density is sufficiently small at the corner of the triangular defect, as shown in Fig. 7. When l is small, the effect of the armchair edge should be dominant and the spin polarization should vanish because the length of the zigzag edge part is short. Therefore, (l, L) graphene exhibits spin polarization when l is large.

We also found that the energy difference per atom between the AM and NM states monotonically increases with l when W is fixed. When l is very large with a fixed W, (l, L) graphene can be regarded almost as a collection of graphene zigzag nanoribbons having AM ground states [63], which is consistent with the present results. Further, we show the total energy difference $\Delta E = E^{\rm tot}_{\rm FM} - E^{\rm tot}_{\rm AM}$, where $E^{\rm tot}_{\rm FM}$ and $E^{\rm tot}_{\rm AM}$ are the total energies of the FM and AM states, respectively, listed in Table IV. It was found that ΔE is smaller for larger W with $l = 11$. It has been reported that when graphene islands are embedded in the h-BN sheet, ΔE monotonically decreases with the distance between islands and approaches zero when the size of islands is fixed [69]. ΔE of (l, L) graphene should behave in the same way because the spin density near (far from) the zigzag edges is large (small). Therefore, ΔE should be so small that (l, L) graphene is NM at room temperature when $L(W)$ is sufficiently large. Hence, the electronic properties of not only the spin-polarized but also the spin-unpolarized states are important, even in the magnetic-ground state cases.

TABLE IV. Total energy differences between FM and AM states ($\Delta E = E^{\rm tot}_{\rm FM} - E^{\rm tot}_{AM}$) of the (l, L) graphenes ($W = L - l$).

l	W	ΔE (eV)
11	2	0.236
9	5	0.214
10	5	0.161
11	5	0.184

2. Band gap values

In Fig. 8, the E_g values of NM, FM, and AM (l, L) graphenes are shown. The E_g values of the AM and FM states nearly converge to nonzero values when W is 2 and 5. This AM tendency can be observed in graphene with periodically arranged hexagonal defects [27]. The E_g values of (11,13) AM graphene ($W = 2$) and (11,16) AM graphene ($W = 5$) are 0.510 and 0.475 eV, respectively. Therefore, (l, L) (W=2,5) AM graphene should be the semiconductor with the E_g value of nearly 0.5 eV when l is large. If the (l, L) (W=2,5) AM graphene with a large l is realized, the E_g value may be larger than 1 eV because the GGA band gap is usually smaller than the actual value.

The E_g values of FM graphene may depend more explicitly on the W value. The E_g values of (11,13) FM graphene and (11,16) FM graphene are 0.669 (MJ) [0.652 (MN)] eV and 0.349 (MJ) [0.277 (MN)] eV, respectively. Here, MJ and MN represent the majority and minority spins, respectively. It is

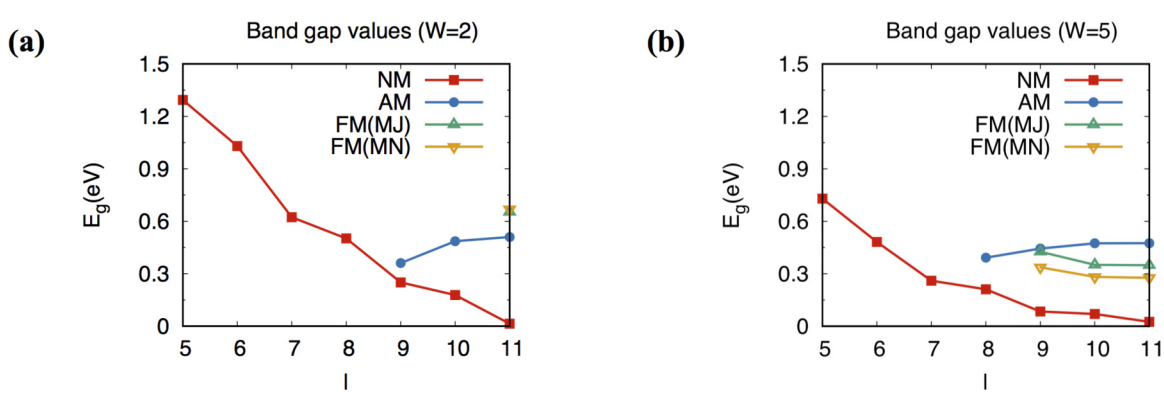

FIG. 8. Band gap (E_g) values of the NM, AM, and FM states when (a) W=2 and (b) W=5. The green and yellow triangles represent the fundamental gap of the majority spin and minority spin, respectively. It is to be noted that $W = L - l$.

expected that the (l,5) FM graphenes with large l have E_g values of about 0.35 eV (MJ) and 0.30 eV (MN).

V. SUMMARY

We have studied the electronic properties of graphenes with truncated triangular defects in superhoneycomb arrangements using the first-principles total-energy calculations based on DFT. It is found that dependence of the band gap (E_g) value on the geometrical parameters in spin-unpolarized systems is different from the scaling law proposed by Pedersen *et al.*, $E_g \propto \sqrt{N_{\rm rem}}/N_{\rm tot}$, which has been widely used. We studied the E_g values for various [l (defect side length), L (supercell size)] and revealed that the E_g values nearly follow the linear function of not $\sqrt{N_{\rm rem}}/N_{\rm tot}$ but $1/(l \times L^2)$, which is roughly proportional to $1/(\sqrt{N_{\rm rem}} \times N_{\rm tot})$. This scaling law should give us the opportunity to design unique device materials and indicates that many interesting electronic properties of graphene with defects still need to be explored. E_g is found to be mostly direct; therefore, the system should be useful for optoelectronic applications. The interplay between the effect of the periodical defects studied in the present paper and the finite size effect would be an interesting issue to be studied in the future when this semiconductor graphene is going to be used in a nanometer scale device. Finally, we investigate the magnetic states by performing spin-polarized calculations. The stable magnetic state could be tuned by changing l with a fixed subribbon width (W). FM and AM stable states are obtained for larger values of l. We find that the E_g values of the AM and FM states converge to nonzero values when l increases. These achievements are significant because the E_g values of large systems cannot be obtained directly from high-cost DFT calculations. The present paper confirms that graphene with honeycomb-arrangement triangular defects is a unique class of semiconducting atomic layers with tunable E_g values. Therefore, van der Waals heterostructures are worthy of further investigation owing to nearly perfect lattice matching, a feature unachievable in typical van der Waals heterostructures [70].

ACKNOWLEDGMENTS

This work was partly supported by JSPS KAKENHI (Grant No. JP19H01823). All numerical calculations were performed using the TSUBAME supercomputer at the Tokyo Institute of Technology.

[1] P. R. Wallace, The band theory of graphite, Phys. Rev. **71**, 622 (1947).
[2] Y. Zheng and T. Ando, Hall conductivity of a two-dimensional graphite system, Phys. Rev. B **65**, 245420 (2002).
[3] H. Suzuura and T. Ando, Anderson localization in a graphene sheet, J. Phys. Soc. Jpn. **72**, 69 (2003).
[4] K. S. Novoselov, A. K. Geim, S. V. Morozov, D.-E. Jiang, Y. Zhang, S. V. Dubonos, I. V. Grigorieva, and A. A. Firsov, Electric field effect in atomically thin carbon films, Science **306**, 666 (2004).
[5] Y.-W. Tan, Y. Zhang, K. Bolotin, Y. Zhao, S. Adam, E. H. Hwang, S. Das Sarma, H. L. Stormer, and P. Kim, Measurement of Scattering Rate and Minimum Conductivity in Graphene, Phys. Rev. Lett. **99**, 246803 (2007).
[6] S. V. Morozov, K. S. Novoselov, M. I. Katsnelson, F. Schedin, D. Elias, J. A. Jaszczak, and A. K. Geim, Giant Intrinsic Carrier Mobilities in Graphene and Its Bilayer, Phys. Rev. Lett. **100**, 016602 (2008).
[7] A. A. Balandin, S. Ghosh, W. Bao, I. Calizo, D. Teweldebrhan, F. Miao, and C. N. Lau, Superior thermal conductivity of single-layer graphene, Nano Lett. **8**, 902 (2008).
[8] K. S. Novoselov, Z. Jiang, Y. Zhang, S. Morozov, H. L. Stormer, U. Zeitler, J. Maan, G. Boebinger, P. Kim, and A. K. Geim, Room-temperature quantum Hall effect in graphene, Science **315**, 1379 (2007).
[9] X. Huang, Z. Yin, S. Wu, X. Qi, Q. He, Q. Zhang, Q. Yan, F. Boey, and H. Zhang, Graphene-based materials: Synthesis, characterization, properties, and applications, Small **7**, 1876 (2011).
[10] R. S. Edwards and K. S. Coleman, Graphene synthesis: relationship to applications, Nanoscale **5**, 38 (2013).
[11] T. Matsumoto and S. Saito, Geometric and electronic structure of new carbon-network materials: Nanotube array on graphite sheet, J. Phys. Soc. Jpn. **71**, 2765 (2002).
[12] O. V. Yazyev and L. Helm, Defect-induced magnetism in graphene, Phys. Rev. B **75**, 125408 (2007).
[13] D. Yu, E. M. Lupton, H. Gao, C. Zhang, and F. Liu, A unified geometric rule for designing nanomagnetism in graphene, Nano Res. **1**, 497 (2008).
[14] D. Yu, E. M. Lupton, M. Liu, W. Liu, and F. Liu, Collective magnetic behavior of graphene nanohole superlattices, Nano Res. **1**, 56 (2008).
[15] T. G. Pedersen, C. Flindt, J. Pedersen, N. A. Mortensen, A.-P. Jauho, and K. Pedersen, Graphene Antidot Lattices: Designed Defects and Spin Qubits, Phys. Rev. Lett. **100**, 136804 (2008).
[16] W. Liu, Z. F. Wang, Q. W. Shi, J. Yang, and F. Liu, Band-gap scaling of graphene nanohole superlattices, Phys. Rev. B **80**, 233405 (2009).
[17] J. A. Fürst, T. G. Pedersen, M. Brandbyge, and A.-P. Jauho, Density functional study of graphene antidot lattices: Roles of geometrical relaxation and spin, Phys. Rev. B **80**, 115117 (2009).
[18] R. Martinazzo, S. Casolo, and G. F. Tantardini, Symmetry-induced band-gap opening in graphene superlattices, Phys. Rev. B **81**, 245420 (2010).
[19] X. Y. Cui, R. K. Zheng, Z. W. Liu, L. Li, B. Delley, C. Stampfl, and S. P. Ringer, Magic numbers of nanoholes in graphene: Tunable magnetism and semiconductivity, Phys. Rev. B **84**, 125410 (2011).
[20] H.-X. Yang, M. Chshiev, D. W. Boukhvalov, X. Waintal, and S. Roche, Inducing and optimizing magnetism in graphene nanomeshes, Phys. Rev. B **84**, 214404 (2011).
[21] R. Petersen, T. G. Pedersen, and A.-P. Jauho, Clar sextet analysis of triangular, rectangular, and honeycomb graphene antidot lattices, ACS Nano **5**, 523 (2011).
[22] F. Ouyang, S. Peng, Z. Liu, and Z. Liu, Bandgap opening in graphene antidot lattices: The missing half, ACS Nano **5**, 4023 (2011).

[23] H. Şahin and S. Ciraci, Structural, mechanical, and electronic properties of defect-patterned graphene nanomeshes from first principles, Phys. Rev. B **84**, 035452 (2011).
[24] M. Sakurai, Y. Sakai, and S. Saito, Electronic properties of graphene and boron-nitride based nanostructured materials, J. Phys. Conf. Ser. **302**, 012018 (2011).
[25] W. Oswald and Z. Wu, Energy gaps in graphene nanomeshes, Phys. Rev. B **85**, 115431 (2012).
[26] M. Dvorak, W. Oswald, and Z. Wu, Bandgap opening by patterning graphene, Sci. Rep. **3**, 2289 (2013).
[27] M. L. Trolle, U. S. Møller, and T. G. Pedersen, Large and stable band gaps in spin-polarized graphene antidot lattices, Phys. Rev. B **88**, 195418 (2013).
[28] J. Lee, A. K. Roy, J. L. Wohlwend, V. Varshney, J. B. Ferguson, W. C. Mitchel, and B. L. Farmer, Scaling law for energy bandgap and effective electron mass in graphene nano mesh, Appl. Phys. Lett. **102**, 203107 (2013).
[29] Z. T. Esfahani, A. Saffarzadeh, and A. Akhound, A dft study on the electronic and magnetic properties of triangular graphene antidot lattices, Eur. Phys. J. B **91**, 308 (2018).
[30] T. Kariyado, Y.-C. Jiang, H. Yang, and X. Hu, Counterpropagating topological interface states in graphene patchwork structures with regular arrays of nanoholes, Phys. Rev. B **98**, 195416 (2018).
[31] E. Nakhmedov, E. Nadimi, S. Vedaei, O. Alekperov, F. Tatardar, A. I. Najafov, I. I. Abbasov, and A. M. Saletsky, Vacancy mediated magnetization and healing of a graphene monolayer, Phys. Rev. B **99**, 125125 (2019).
[32] B. Sakkaki, H. R. Saghai, G. Darvish, and M. Khatir, Electronic and optical properties of passivated graphene nanomeshes: An ab initio study, Opt. Mater. (Amsterdam) **122**, 111707 (2021).
[33] J. Eroms and D. Weiss, Weak localization and transport gap in graphene antidot lattices, New J. Phys. **11**, 095021 (2009).
[34] A. J. M. Giesbers, E. C. Peters, M. Burghard, and K. Kern, Charge transport gap in graphene antidot lattices, Phys. Rev. B **86**, 045445 (2012).
[35] A. Sandner, T. Preis, C. Schell, P. Giudici, K. Watanabe, T. Taniguchi, D. Weiss, and J. Eroms, Ballistic transport in graphene antidot lattices, Nano Lett. **15**, 8402 (2015).
[36] J. Bai, X. Zhong, S. Jiang, Y. Huang, and X. Duan, Graphene nanomesh, Nat. Nanotechnol. **5**, 190 (2010).
[37] M. Kim, N. S. Safron, E. Han, M. S. Arnold, and P. Gopalan, Fabrication and characterization of large-area, semiconducting nanoperforated graphene materials, Nano Lett. **10**, 1125 (2010).
[38] M. Kim, N. S. Safron, E. Han, M. S. Arnold, and P. Gopalan, Electronic transport and raman scattering in size-controlled nanoperforated graphene, ACS Nano **6**, 9846 (2012).
[39] L. Liu, Y. Zhang, W. Wang, C. Gu, X. Bai, and E. Wang, Nanosphere lithography for the fabrication of ultranarrow graphene nanoribbons and on-chip bandgap tuning of graphene, Adv. Mater. **23**, 1246 (2011).
[40] R. K. Paul, S. Badhulika, N. M. Saucedo, and A. Mulchandani, Graphene nanomesh as highly sensitive chemiresistor gas sensor, Anal. Chem. **84**, 8171 (2012).
[41] M. Wang, L. Fu, L. Gan, C. Zhang, M. Rümmeli, A. Bachmatiuk, K. Huang, Y. Fang, and Z. Liu, Cvd growth of large area smooth-edged graphene nanomesh by nanosphere lithography, Sci. Rep. **3**, 1238 (2013).
[42] A. Esfandiar, N. J. Kybert, E. N. Dattoli, G. Hee Han, M. B. Lerner, O. Akhavan, A. Irajizad, and A. Charlie Johnson, Dna-decorated graphene nanomesh for detection of chemical vapors, Appl. Phys. Lett. **103**, 183110 (2013).
[43] X. Zhu, W. Wang, W. Yan, M. B. Larsen, P. Bøggild, T. G. Pedersen, S. Xiao, J. Zi, and N. A. Mortensen, Plasmon–phonon coupling in large-area graphene dot and antidot arrays fabricated by nanosphere lithography, Nano Lett. **14**, 2907 (2014).
[44] X. Liang, Y.-S. Jung, S. Wu, A. Ismach, D. L. Olynick, S. Cabrini, and J. Bokor, Formation of bandgap and subbands in graphene nanomeshes with sub-10 nm ribbon width fabricated via nanoimprint lithography, Nano Lett. **10**, 2454 (2010).
[45] B. Zribi, J.-M. Castro-Arias, D. Decanini, N. Gogneau, D. Dragoe, A. Cattoni, A. Ouerghi, H. Korri-Youssoufi, and A.-M. Haghiri-Gosnet, Large area graphene nanomesh: An artificial platform for edge-electrochemical biosensing at the sub-attomolar level, Nanoscale **8**, 15479 (2016).
[46] M. E. Schmidt, T. Iwasaki, M. Muruganathan, M. Haque, H. Van Ngoc, S. Ogawa, and H. Mizuta, Structurally controlled large-area 10 nm pitch graphene nanomesh by focused helium ion beam milling, ACS Appl. Mater. Interfaces **10**, 10362 (2018).
[47] F. Liu, Z. Wang, S. Nakanao, S. Ogawa, Y. Morita, M. Schmidt, M. Haque, M. Muruganathan, and H. Mizuta, Conductance tunable suspended graphene nanomesh by helium ion beam milling, Micromachines **11**, 387 (2020).
[48] C. Jin, F. Lin, K. Suenaga, and S. Iijima, Fabrication of a Freestanding Boron Nitride Single Layer and Its Defect Assignments, Phys. Rev. Lett. **102**, 195505 (2009).
[49] M. Kim, S. W. Moon, G. Kim, S. I. Yoon, K. Kim, S. K. Min, and H. S. Shin, Effect of pt crystal surface on hydrogenation of monolayer h-BN and its conversion to graphene, Chem. Mater. **32**, 4584 (2020).
[50] P. Hohenberg and W. Kohn, Inhomogeneous electron gas, Phys. Rev. **136**, B864 (1964).
[51] W. Kohn and L. J. Sham, Self-consistent equations including exchange and correlation effects, Phys. Rev. **140**, A1133 (1965).
[52] J. P. Perdew, K. Burke, and M. Ernzerhof, Generalized Gradient Approximation Made Simple, Phys. Rev. Lett. **77**, 3865 (1996).
[53] J. P. Perdew, K. Burke, and M. Ernzerhof, Errata: Generalized Gradient Approximation Made Simple (1996), Phys. Rev. Lett. **78**, 1396(E) (1997).
[54] D. Vanderbilt, Soft self-consistent pseudopotentials in a generalized eigenvalue formalism, Phys. Rev. B **41**, 7892 (1990).
[55] P. Giannozzi, S. Baroni, N. Bonini, M. Calandra, R. Car, C. Cavazzoni, D. Ceresoli, G. L. Chiarotti, M. Cococcioni, I. Dabo *et al.*, Quantum Espresso: A modular and open-source software project for quantum simulations of materials, J. Phys.: Condens. Matter **21**, 395502 (2009).
[56] K. Momma and F. Izumi, Vesta: A three-dimensional visualization system for electronic and structural analysis, J. Appl. Crystallogr. **41**, 653 (2008).
[57] J. Ito, J. Nakamura, and A. Natori, Semiconducting nature of the oxygen-adsorbed graphene sheet, J. Appl. Phys. **103**, 113712 (2008).
[58] K. Kanamitsu and S. Saito, Geometries, electronic properties, and energetics of isolated single walled carbon nanotubes, J. Phys. Soc. Jpn. **71**, 483 (2002).
[59] Y. Fujimoto and S. Saito, Formation, stabilities, and electronic properties of nitrogen defects in graphene, Phys. Rev. B **84**, 245446 (2011).

[60] Y. Sakai, S. Saito, and M. L. Cohen, Lattice matching and electronic structure of finite-layer graphene/h-BN thin films, Phys. Rev. B **89**, 115424 (2014).

[61] T. Haga, Y. Fujimoto, and S. Saito, Electronic structure and scanning tunneling microscopy images of heterostructures consisting of graphene and carbon-doped hexagonal boron nitride layers, Phys. Rev. B **100**, 125403 (2019).

[62] See Supplemental Material at http://link.aps.org/supplemental/10.1103/PhysRevB.107.235418 for detailed structure of defects, bond lengths, electronic structures, and wave functions.

[63] Y.-W. Son, M. L. Cohen, and S. G. Louie, Energy Gaps in Graphene Nanoribbons, Phys. Rev. Lett. **97**, 216803 (2006).

[64] L. Yang, C.-H. Park, Y.-W. Son, M. L. Cohen, and S. G. Louie, Quasiparticle Energies and Band Gaps in Graphene Nanoribbons, Phys. Rev. Lett. **99**, 186801 (2007).

[65] M. Ezawa, Peculiar width dependence of the electronic properties of carbon nanoribbons, Phys. Rev. B **73**, 045432 (2006).

[66] M. Y. Han, B. Özyilmaz, Y. Zhang, and P. Kim, Energy Band-Gap Engineering of Graphene Nanoribbons, Phys. Rev. Lett. **98**, 206805 (2007).

[67] E. H. Lieb, Two Theorems on The Hubbard Model, Phys. Rev. Lett. **62**, 1201 (1989).

[68] M. Fujita, K. Wakabayashi, K. Nakada, and K. Kusakabe, Peculiar localized state at zigzag graphite edge, J. Phys. Soc. Jpn. **65**, 1920 (1996).

[69] A. Ramasubramaniam and D. Naveh, Carrier-induced antiferromagnet of graphene islands embedded in hexagonal boron nitride, Phys. Rev. B **84**, 075405 (2011).

[70] Y. Taguchi, M. Toyoda, and S. Saito, *Band Engineering and Quantum Well Formation in Semiconducting Defective Graphene Multilayers—A First-Principles Study*, Materials Research Society 2021 Fall Meeting, **EQ20.22.02**, Abstract book p. 972, https://www.mrs.org/docs/default-source/meetings-events/fall-meetings/2021/abstract-book.pdf.